Validation of gas flow experiments for porous media by means of computer simulations

OPEN ACCESS
IOP Publishing
Measurement Science and Technology
Meas. Sci. Technol. **34** (2023) 045012 (18pp)
https://doi.org/10.1088/1361-6501/acb373

Validation of gas flow experiments for porous media by means of computer simulations

Sunny Laddha[1,*], Wolfgang Macher[1], Günter Kargl[1], Stephan Zivithal[1], Jürgen Blum[2], Bastian Gundlach[2], Carsten Güttler[3], Holger Sierks[3] and Martin Rose[4]

[1] Space Research Institute, Austrian Academy of Sciences, Schmiedlstrasse 6, A-8042 Graz, Austria
[2] Institut für Geophysik und extraterrestrische Physik (IGeP), TU Braunschweig, Mendelssohnstr. 3, 38106 Braunschweig, Germany
[3] Max-Planck-Institut für Sonnensystemforschung, Justus-von-Liebig-Weg 3, 37077 Göttingen, Germany
[4] Ingenieurbuero Dr-Ing. Martin Rose, Sommerhofenstrasse 148, 71067 Sindelfingen, Germany

E-mail: sunny.laddha@oeaw.ac.at

Received 15 September 2022, revised 18 December 2022
Accepted for publication 16 January 2023
Published 30 January 2023

Abstract

A profound understanding of gas flow in porous media is of great interest for various technological and scientific fields. Its investigation by laboratory measurements, however, poses several challenges. In particular, the determination of macroscopic flow parameters from pressure and gas flow measurements is prone to various error influences, some of which are very difficult to analyze experimentally. Computer simulations are a solution in this context as they facilitate modifications of the underlying geometry and boundary conditions in a flexible way. Here we present a simulation framework for the analysis of a recent experiment for determining the Knudsen diffusion coefficient and viscous permeability of various porous granular materials. By combining the finite element method with analytical models and other numerical methods, we were able to identify previously neglected physical effects that increase the uncertainty of the measurements. In particular, the porosity increase due to finite sample dimensions, in a layer of about a grain diameter thickness near the container wall, creates a deviation of the measured pressure gradient. This deviation amounts to ca. 5% for a sample width of about 100 grains and a porosity of 0.5, and is indirectly proportional to the porosity. The second most prominent error source, the sample support sieve, causes a slight constriction of the flow volume. Simulations of this effect show an error around 4%–7%, dependent on the grain size. Based on these findings we recommend an overall sample dimension of 100 grains or larger. As an example of failures of the sample homogeneity, we elaborate how channels through the sample influence the flow properties. Respective suggestions for keeping all discussed effects negligible are discussed in detail. Our methodology demonstrates how the combination of finite element computations with analytical representations of the involved macroscopic parameters can assess the validity and accuracy of laboratory experiments.

* Author to whom any correspondence should be addressed.

Keywords: gas flow, porous media, measurement validation

(Some figures may appear in colour only in the online journal)

1. Introduction

The treatment of the theory of gas flow through porous media is as versatile as its application in technological and scientific fields. In most applications the transition from viscous gas flow to Knudsen diffusion, where the mean free path of gas molecules is longer than the typical pore size, plays an essential role. It is of great relevance for important technical developments of the last century, like catalysts (Satterfield 1970) and fuel cells (Pant *et al* 2012), but also for petrochemistry (e.g. shale gas extraction (Chen *et al* 2017)) and space sciences (e.g. outgassing of volatiles from comets and other bodies (Gundlach *et al* 2011, Skorov *et al* 2011, Schweighart *et al* 2021, Haack 2022)). In the industrial field, the value of improving the comprehension of the underlying physics becomes evident in the form of immediate technological advancement. In space sciences, it contributes to the long-term challenge of better understanding processes in the near-surface layers of solid space bodies, in particular of comets, the primordial building blocks of our Solar System. Since cometary activity is partly driven by release of volatile substances through the highly porous surface material, the gas flow through the pores is a crucial aspect in this context, too.

The present work originated from this application in space science, but it is pertinent to all other fields where gas flow through porous media plays a role, such as the mentioned technological examples. Remote observations and even more *in-situ* measurements of phenomena on space bodies like comets are extremely difficult and expensive (a multitude of instruments onboard of satellites and landers/rovers are needed for this purpose). So experiments in a controlled laboratory environment, using artificial and analog materials, are indispensable for the study of the relevant processes. Such experiments have been conducted by various authors over the years (e.g. the first large-scale campaign 'KOSI-Kometensimulation'—see Grün *et al* 1991, 1992), however, often too many parameters were varied simultaneously. This impedes the isolated analysis of different effects and makes a direct comparison with numerical models (Benkhoff and Spohn 1991, Prialnik 1991, Steiner *et al* 1991), which were developed in parallel to these experiments, difficult.

To address still unanswered questions with an improved methodology and incorporate state-of-the-art knowledge gained from the most recent cometary space mission *Rosetta* (Barucci and Fulchignoni *et al* 2017), a new research campaign dedicated to cometary physics was initiated in 2018. The international consortium *CoPhyLab* ('Comet Physics Laboratory'), in the framework of which this work was carried out, featured the development and construction of a highly specialized vacuum chamber by Kreuzig *et al* (2021). In parallel several small-scale experiments were carried out by the team to determine the thermal, optical, electrical and mechanical properties of cometary analog materials (Bischoff *et al* 2018, Gundlach *et al* 2018, 2020, Haack *et al* 2020, 2021, Haack 2022). One kind of these experiments was conceived for analyzing gas flow through dry cometary analog material (Schweighart *et al* 2021). Ice-dust mixtures were intentionally omitted to focus on the pure gas transport through pores without complicating heat transfer and sublimation/condensation effects. Similar to *KOSI*, also the *CoPhyLab* experiments are accompanied by numerical models.

Owing to significant advances in computer technology in the last decades, much more complicated mathematical models can be applied and higher levels of detail are achievable now. Even the detailed structure of pores can be roughly modeled nowadays with particle codes such as the lattice Boltzmann methods (van Doormaal and Pharoah 2009) or, for rarified gas flow, Direct Simulation Monte Carlo (DSMC) algorithms (Christou *et al* 2020). However, these models require excessive computation time even for a small packing of grains. Further, DSMC usually yields high standard deviations in predicted macroscopic quantities due the stochastic approach, and produces a plethora of output on gas molecule motion, which is not always required. To conduct the validation of the above mentioned experiment by Schweighart *et al* (2021) with computer simulations, we decided in favor of the finite element method (FEM). The justification for this choice is that the binary friction model (BFM), which was used in the evaluation of the experiment (and also in other cases by Kast and Hohenthanner 2000, Pant *et al* 2012), can be implemented in a resource-efficient manner by the FEM.

The BFM approximates the flow through a porous medium by two additive terms corresponding to Knudsen diffusion and viscous flow. It is applicable to a wide range of pressures, from the Knudsen to the viscous regime, whereby the flow is characterized by macroscopic flow parameters (the Knudsen diffusion coefficient D^{K} and the viscous permeability B). These parameters can be derived from the characteristics of the porous medium or grain packing by means of various 'microscopic' models of the pore/grain structure. It is crucial to validate if these models match the observations with sufficient accuracy, which was done by various authors like Asaeda *et al* (1974) and Pant *et al* (2012). However, as the models are only as good as the parameters which they are based on, it is also necessary to scrutinize the uncertainties that typically appear in the measurement of D^{K} and B. In section 3.4 of their work, Schweighart *et al* (2021) discussed various errors encountered in the experiment in terms of the standard definitions of uncertainties (ISO/IEC Guide 98-3:2008 2010). Nevertheless, when the aim is to extract parameters with complex dependencies such as D^{K} and B, there are some uncertainties related to physical effects and the assumptions made by the observer, that cannot be easily addressed by a formal error analysis. Furthermore, the nature of said uncertainties can be specific to the

measurement methods, which themselves are very versatile (see experiments by Wu *et al* 1998, Miguel and Serrenho 2007 and the comprehensive review by Sharma and Siginer 2010).

To differentiate between uncertainties due to the experimental setup and those related to physical effects, we propose a simulation framework (section 2) in which the gas flow experiment is replicated numerically with the FEM. A similar approach was successfully employed by Larsson *et al* (2020), albeit for a different field (flow of granular media itself). On the one hand, this enables a direct comparison of the simulation results with the measurements for the validation of the underlying mathematical model (section 3). On the other hand, it demonstrates in a more general way, how the combination of analytical and numerical methods (sections 3.3 and 4) can assist in the identification of the sources of discrepancies. To our knowledge, some of these error sources have not been discussed in a laboratory measurement context so far and are extremely difficult to analyze purely experimentally. Although our findings (as summarized in section 5) may be specific to the presented experimental setup, they prove the effectiveness of the used methodology, which can also be applied in other fields, and highlight potential areas of improvement for future gas flow measurements.

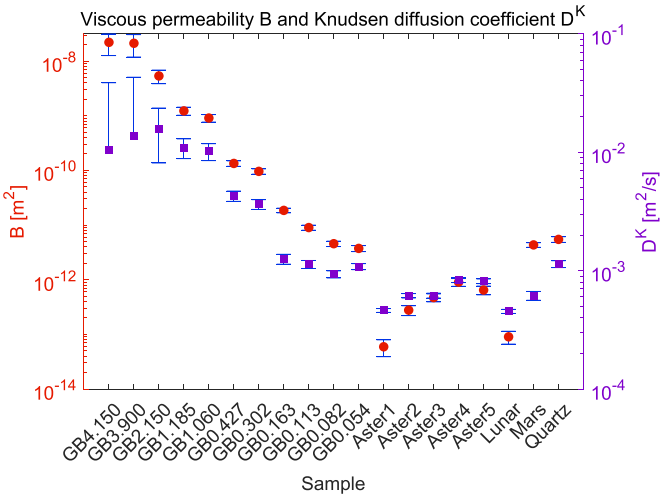

Figure 1. Viscous permeability B and Knudsen diffusion coefficient D^{K} for glass beads and analog materials as obtained by Schweighart *et al* (2021) by means of laboratory experiments. One-sided error bars indicate that only an estimate of the order of magnitude was achieved for the respective value. The numbers following the letters GB refer to the average grain diameter of the respective group in millimeters.

2. Experimental and simulation framework

2.1. Measurement setup

The numerical simulations of this work are based on the laboratory experiments conceived by Schweighart *et al* (2021) to simultaneously determine the viscous permeability B and the Knudsen diffusion coefficient D^{K} of different glass bead fractions and of planetary and cometary analog materials. We refer to their work for a detailed description but will summarize the most important aspects here, as they are necessary to establish a framework for the simulations. The main results are shown in figure 1, which is used as a reference below. The numbers following the letters glass beads (GB) in the figure refer to the average grain diameter of the respective group in millimeters. The same nomenclature is also applied in the following figures. The main part of the setup, as illustrated in figure 2, is a small vacuum chamber composed of two compartments. They are joined by a sample holder so that the gas flow from the upper to the lower compartment is forced through the sample. The sample holder is a cylindrical tube which can be filled with material up to a height of roughly 35 mm. A sieve at the cylinder base prevents the sample materials from falling down. The chamber is evacuated by a vacuum pump that is attached to the lower compartment beneath the sample (henceforth referred to as downstream compartment), while gas flow is introduced into the upper compartment (upstream compartment). In the presence of a sample inside the container, a pressure difference develops between the compartments depending on the gas permeability of the sample. Identical sets of sensors measure the up- and downstream compartment pressures, p_{u} and p_{d}, simultaneously. To achieve sufficient accuracy over the whole pressure range, different types of sensors

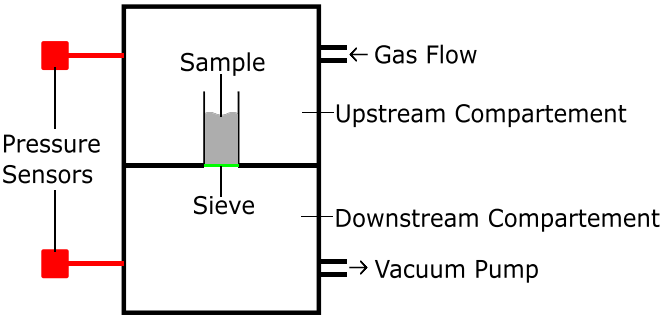

Figure 2. Schematic of the experimental setup. The sample is held inside a vacuum chamber by a cylindrical container and a sieve. Gas flow is input to the upper compartment by a flow controller and evacuated from the lower compartment by a vacuum pump. The gas flow rate and the pressure in both volumes are monitored.

were employed. The gas flow rate was controlled with a commercial regulator, which was operated by the same software interface as the pressure sensors. The transition time from one flow setting to the next was usually shorter than the time cadence of the measurements, except for the highest flow setting which required slightly more time. For a controlled repeatability, the gas flow rate was always started with the lowest setting, and afterwards stepped up to higher flow rates once steady-state pressures were achieved in both compartments. The gas used in these experiments was dry, water- and oil-free compressed air at room temperature.

2.2. Sample materials

The samples used for these experiments were a selection of natural and artificial materials. All natural materials were typically mined from a quarry and subsequently crushed and

milled down to smaller particle fractions. An exception is the UCF/DSI-CI-2 Asteroid analog material, which consists of a mix of selected minerals based on the Orgueil CI carbonaceous chondrite meteorite (see Bland *et al* 2004, Britt *et al* 2019 for details). All natural materials except the asteroid analog were sieved for a maximum grain size $d_{\text{grain}} < 1$ mm. For a further characterization, the grain size distribution was determined using multiple sieves based on the ISO 3310-1:2016 (2016) and ASTM E11 *et al* (2017) standard, with a grading (inner mesh width of the grid) of 1 mm down to 0.45 µm. A good portion of the measurements were performed with beads of polished soda lime glass (henceforth named glass beads or GB) with a narrow size distribution, since they have a well-defined shape and size, are readily available and often used as reference material. Because of their high sphericity (measure of roundness, with values between 0–non-spherical and 1–perfect sphere), samples of homogeneous packing can be produced with better repeatability. GB below 250 µm and all natural materials are more angular, making samples prone to local failure of homogeneity, which may influence the sample permeability considerably. Thus, for all samples with angular grains and/or small grain fractions, the sample has to be carefully prepared to ensure repeatable measurements. Further details are discussed below and by Schweighart *et al* (2021).

2.3. Simulation method and software

The evaluation of the measurements yields a set of material specific parameters that describe the gas flow properties of a sample macroscopically, making it suitable for a finite element analysis (FEA). The inherent assumption of this approach is that the sample is homogeneous and isotropic. We chose the software *COMSOL Multiphysics*® as it offers a complete workflow, from geometry design to post processing, with a user-friendly interface. A wide range of modules for different physical problems and various numerical solvers make it a versatile simulation tool. In the present context the Heat Transfer and the Porous Media Flow modules can be used.

2.3.1. Governing differential equations. The BFM gas flow model was implemented in *COMSOL* by an adaptation of Darcy's law, which relates the pressure gradient ∇p in a fluid percolating through a porous medium to the filtration velocity $\mathbf{u}$ (that is the fluid velocity outside the pores when the fluid would exit the medium at the respective location, which equals the locally averaged pore velocity times the medium porosity),

$$\mathbf{u} = -\frac{B_{\text{t}}}{\mu}\nabla p, \tag{1}$$

with permeability B_{t} and dynamic viscosity μ of the fluid. This relation is available in the above mentioned 'Porous Media Flow' module. For viscous flow B_{t} is constant over a wide range of pressures and represents the solid-pore properties, whereas μ represents the fluid. However, since we consider a gas fluid, we have to take into account that the character of the flow changes, if the pressure declines sufficiently for the gas molecules to collide with the pore surfaces more often than with each other. In the ultimate case the molecule-molecule collisions are so rare that they can be neglected in comparison with the molecule-pore surface collisions (Knudsen pressure regime). In this case only a Knudsen diffusion flux (flow rate per cross-sectional area)

$$\mathbf{J} = n\,\mathbf{u} = -D^{\text{K}}\,\nabla n \tag{2}$$

is present, caused by a gradient ∇n of the molar gas density n. Writing this equation in the form of equation (1) for the filtration velocity shows that B_{t} changes with density (i.e. with pressure in virtue of the ideal gas law). There is a wide transition region between the pure viscous and Knudsen regimes, where the permeability depends on the pressure. A good approximation is given by the BFM, which regards the total gas flow as the sum of Knudsen diffusion and pure viscous flow (Kast and Hohenthanner 2000, Pant *et al* 2012). In accordance with the BFM the total permeability B_{t} can be written as

$$B_{\text{t}} = B + \frac{\mu D^{\text{K}}}{p}, \tag{3}$$

where B represents the permeability for the pure viscous flow contribution. This BFM approach was also applied by Schweighart *et al* (2021) for isothermal conditions, implying constant viscosity throughout the sample. The second governing equation of the model is the continuity equation

$$Q = \frac{\partial}{\partial t}(\epsilon n) + \nabla \cdot (n\mathbf{u}), \tag{4}$$

where Q describes the density of a potential particle source and ϵ the porosity of the solid phase. It should be noted that $Q = 0$ for all simulations, because in the present application the mass source is external and so sources can be regarded as taken into account via the boundary conditions.

2.3.2. Klinkenberg pressure and appropriate pressure ranges. To understand the magnitude of the uncertainties of the measured parameters B and D^{K}, it is important to consider in which pressure range (i.e. flow regime) the measurements were taken. An accurate determination of the Knudsen diffusion coefficient D^{K} is only possible when the contribution of the viscous flow is not too strong. If the pressure is too high, the viscous flow dominates and the contribution of the Knudsen diffusion is so faint that it is of the order of the flux variations, which prevents an accurate determination of D^{K}. Vice versa, an accurate measurement of the viscous permeability B is only possible if its contribution to the total flow is not too small. Thus, a simultaneous determination of both, D^{K} and B, is only possible with high accuracy, if the pressure range covered by all evaluated stationary measurements overlaps with a certain region around the Klinkenberg pressure

$$b^{\text{K}} = \frac{D^{\text{K}}\mu}{B}, \tag{5}$$

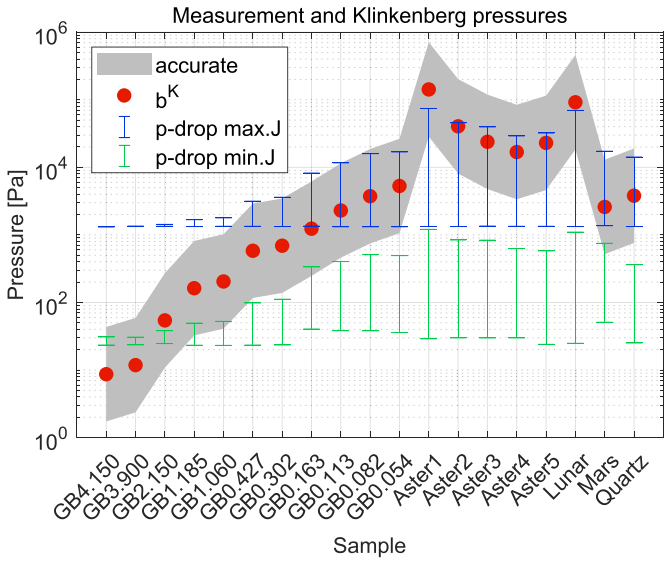

Figure 3. Klinkenberg pressures b^{K} for studied glass beads (GB) and analogs, where the Knudsen diffusion and viscous flow contribute equally to the total flux. An accurate measurement of both, D^{K} and B is guaranteed, when the pressure drop occurring across the sample overlaps with the gray band. Green and blue bars show the pressure drop across each sample, for the minimum and maximum applied gas flow settings, respectively.

where the viscous flow and the Knudsen diffusion contribute equally to the total flux (Klinkenberg 1941). Figure 3 illustrates this region as a gray band, spanned around the Klinkenberg pressures b^{K} (red dots) of the studied samples by a factor of five $(b^{\mathrm{K}}/5, 5\,b^{\mathrm{K}})$. The size of this region depends on the desired accuracy of the flow parameters; here our choice was such that, in the worst case, about a decimal may be lost in accuracy of D^{K} or B when the opposite flow dominates (assuming a simultaneous evaluation of the 8 applied flux settings). The measured pressure differences across the samples are shown as green and blue bars, for the lowest and highest gas flux settings, respectively. We see that the mentioned condition is well fulfilled for most samples, except for Asteroid 1 and the two largest GB samples. For the largest GB an additional, propagated error in the measurement evaluation stems from the extremely small pressure difference across the sample, relative to the average pressure. As a consequence, the D^{K} values cannot be determined with high accuracy under the applied conditions, as the error bars in figure 17 given by Schweighart *et al* (2021) confirm.

2.3.3. Solver settings. Since *COMSOL* provides the complete workflow of an FEA, with most settings predefined so as to work well with many problems, only few explicit solver settings or modifications are needed. Some tasks can cause the program to require excessive amounts of time and memory or even fail to converge to a solution. Under these circumstances, it is essential to adapt the configuration to provide a meaningful solution in terms of accuracy and computational resources. Although the geometry of the studied sample is not complex (cylindric sample on top of a cylinder-symmetric sieve), there are some pitfalls when not paying attention to specific details of the solver settings.

While stationary studies only require a spatial discretization, which is achieved through the creation of a mesh (see section 2.3.5), time-dependent studies also require a temporal discretization. The transient cases studied in the present context do not converge with the explicit Runge-Kutta method, which is a characteristic of stiff problems. Therefore, the backward differentiation formula (BDF), which is an implicit method, was chosen for the transient studies. After building the system of equations, it is solved by either direct or iterative methods. Although the user can select manually, the default settings for predefined physics modules are usually correct. As such, either *MUMPS* or *PARDISO* were chosen from the available direct solvers, according to whichever was more performant. Further, it is important to note that the settings regarding tolerances had to be adapted for certain simulations. After each time step the solver estimates the error of the computed solution and accepts the step only if it satisfies a condition specified by the absolute and relative tolerances defined by the user. In general, when the magnitude of a dependent variable of a problem changes considerably during the run, it is scaled to avoid ill-conditioning. Consequently, the absolute tolerance is also scaled automatically, however this has led to extreme computation times or even failure in some cases. The simulations of section 4.3 are such an example, where the absolute tolerance was therefore set constant and a suitable relative tolerance was introduced to ensure acceptable accuracy.

2.3.4. Boundary conditions. In the simplest case, the simulation sample was modeled as a cylinder with a flat base equal to the cross-section of the sample container used in the experiments by Schweighart *et al* (2021). The cylinder height was set to the height measured from the sample-supporting sieve to the sample top (so all grains of the sample are fully contained in the simulated volume). For the first verification, the material specific parameters B, D^{K} and ϵ as determined by measurements, were directly input to the simulations, so that the time evolution of the pressures should closely resemble the measured ones. The pressure throughout the sample is not only determined by the differential equations governing the flow-pressure relation in the material but also by the boundary conditions. The presence of the sample container was implemented by applying a no-flow condition normal to the cylinder mantle. In addition, conditions had to be defined for the flow entering and leaving the sample. In stationary cases the definition of the flux J in the net flow direction (parallel to the cylinder axis) and one of the compartment pressures (either upstream, p_{u}, or downstream, p_{d}) were sufficient. In general, two of the quantities J, p_{u}, p_{d} determine the solution uniquely.

For the transient problem the situation is more complicated. The volume of the up- and downstream compartments outside the sample play an essential role for the time evolution of the pressure. The volumes cause a pressure response lag when the setting of the gas flow controller or pump is changed. In order to estimate this effect, the compartment volumes and the pump performance curve (as given by the manufacturer) were

implemented in the simulations as follows. The condition at the boundary between the sample and the upstream compartment has to allow for a change of gas flow due to the gas buffering in the upstream compartment

$$\dot{p}_\mathrm{u} = \frac{RT}{MV_\mathrm{u}}\,(F_\mathrm{in} - F_\mathrm{u}), \tag{6}$$

where $\dot{p}_\mathrm{u}$ is the pressure change rate in the upstream compartment of volume V_u, R the gas constant, T the temperature, and M the molar mass of the gas. The gas flow F_in through the chamber inlet differs from the flow F_u into the sample when the pressure increases since a certain portion stays (is buffered) in the upstream compartment. On the other hand, when the inflow is stopped ($F_\mathrm{in} = 0$) there is still a flow towards the sample ($F_\mathrm{u} \neq 0$) when the pump remains on, because the gas buffered in V_u is released towards the sample as long as there is a pressure difference across the sample.

Analogously, the condition for the boundary between the sample and the downstream compartment is obtained

$$\dot{p}_\mathrm{d} = \frac{RT}{MV_\mathrm{d}}\,(F_\mathrm{d} - F_\mathrm{out}), \tag{7}$$

where the time-derivative $\dot{p}_\mathrm{d}$ of the pressure at the downstream sample boundary is positive when the gas flow towards the pump (through the outlet of the vacuum chamber) is smaller than the flow from the sample to the downstream compartment. Since the pump is connected to the chamber via a hose of about 1 m length, it is essential to take into account not only the performance of the pump but also the flow resistance of the hose. For most of the evaluated measurement data, the tubular diameter d_h is much larger than the mean free path of the pumped gas, and the flow through the hose can be approximated by the Hagen–Poiseuille law (Shen *et al* 2019) for tubes of circular cross-section

$$\dot{V} = \frac{d_\mathrm{h}^4 \pi}{128\mu}\,\frac{\mathrm{d}p}{\mathrm{d}x}, \tag{8}$$

where d_h is the inner diameter of the hose and $\dot{V}$ the volume flow rate through any cross-section normal to the tube axis (x). This is an approximation, since it only holds strictly for stationary flow. However, the flow inside the tube becomes quasi-stationary quite fast and further changes due to non-stationary flow inside the vacuum chamber (up- and downstream compartments and sample) occur on a much longer time scale, so only negligible errors can be expected due to the stationarity assumption for the flow through the hose. Since the volume flow rate is not constant along the tube, we have to rewrite the above equation in terms of the mass flow rate $F = \dot{V}Mp/(RT)$. Integration of the resulting equation over the hose length L (see also Landau and Lifshitz 1987) yields (utilizing the fact that F is constant for stationary flow)

$$p^2 - p_\mathrm{p}^2 - \frac{256\,\mu RTL}{d_\mathrm{h}^4 \pi M}\,F_\mathrm{out} = 0. \tag{9}$$

Here p_p is the pressure at the pump and p the pressure at the vacuum chamber outlet (connection of the hose), which practically coincides with the downstream pressure p_d. The flow through the hose is determined by the pump performance characteristic $F_\mathrm{out} = F_\mathrm{p}(p_\mathrm{p})$, which gives the flow rate F_p achieved by the pump at given pump pressure p_p.

In the beginning of a measurement set, the chamber was evacuated to pressures of the order of 1 Pa until the flow from the upper compartment practically vanished, and afterwards the flow settings for the different stationary measurements were initialized consecutively. Thereby, only the pressure values of the steady-state (henceforth called pressure plateaus) were used for the final evaluation. Because the flow rates during the transition period to the first (lowest) pressure plateau are extremely small, the molecular diffusion becomes relevant even in the hose between the pump and chamber. An extension of equation (9) to the more general case including Knudsen diffusion can be found with equation (10) from Schweighart *et al* (2021) and the substitution $B = d_\mathrm{h}^2/32$ and $D^\mathrm{K} = d_\mathrm{h}\bar{c}/3$. Rewriting this equation in terms of the pressure p at the hose-chamber connection and the pressure p_p at the pump, reads

$$p^2 - p_\mathrm{p}^2 + 2b^\mathrm{K}(p - p_\mathrm{p}) - \frac{256\mu RTL}{d_\mathrm{h}^4 \pi M}\,F_\mathrm{out} = 0. \tag{10}$$

For the applied hose of 16 mm diameter the Klinkenberg pressure is $b^\mathrm{K} \approx 5.6$ Pa. Figure 4 shows the pump performance and how it changes in dependence of the length of the connected hose (0 m indicates the pump characteristic without a hose). The dashed lines are calculated with equation (9) and the solid ones with equation (10). The effect of the hose of 1 m length is about 20% of $F \approx 1\,\mathrm{mg\,s^{-1}}$ at $p_\mathrm{p} \approx 100$ Pa, becoming considerably larger at lower pressures. However, the Knudsen diffusion mitigates this effect (resistance of the hose to the flow), which would be much more pronounced if only viscous flow were present. The figure also indicates the Klinkenberg pressure and the flow rate F_crit, where the Reynolds number reaches its critical value $\mathrm{Re}_\mathrm{crit} \approx 2000$ above which sustained turbulence can dominate the flow. Since the above derivations assume that the viscous flow is laminar, they are only applicable below this threshold. Figure 4 shows that the laminar calculations are well applicable in the flow range 0.15–20 mg s^{-1} typically covered by our measurements, but would become inaccurate when approaching $F_\mathrm{crit} \approx 460\,\mathrm{mg\,s^{-1}}$.

In contrast to the flow through the hose between the pump and the vacuum chamber, the flow through the sample occurs only in the Knudsen and transition regimes. For the flow conditions simulated here, the Reynolds number is sufficiently small so that the BFM is well applicable. Estimates by Schweighart *et al* (2021) showed that even for samples with the largest grains of about 4 mm diameters a Reynolds number of about five is reached for the highest applied flow rates. They showed that for such samples other measurement errors are much more prominent. So in all examples studied here the viscous flow contribution in the sample (which plays a role in the transition regime) is laminar.

The equations (6), (7) and (10) define the boundary conditions completely if, in addition, the time-dependent inflow $F_\mathrm{in}(t)$ and the pump characteristic $F_\mathrm{p}(p_\mathrm{p})$ are given. Equations (6) and (7) are implemented in the COMSOL simulations as additional (global) ordinary differential equations,

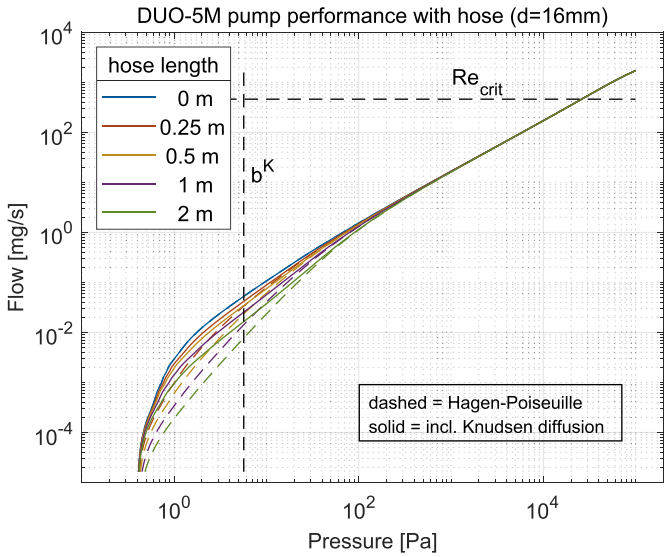

Figure 4. Performance characteristic of the used vacuum pump, showing the flow rate F_p the pump achieves as a function of the pump pressure p_p (blue line). The additional lines include the performance loss due to a connection hose of 16 mm diameter.

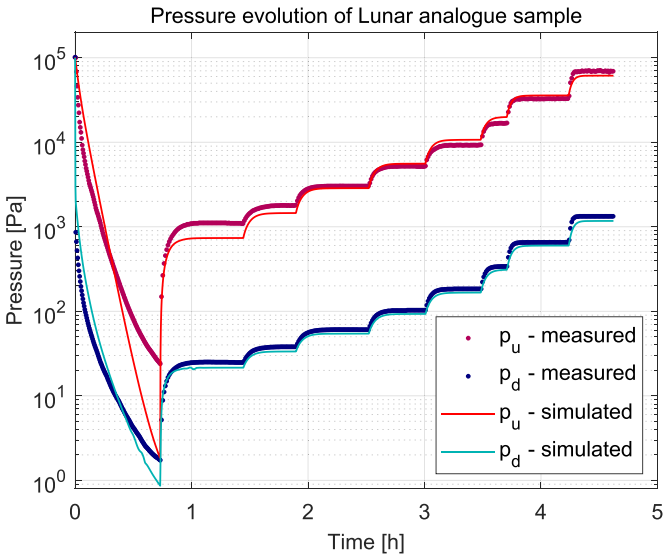

Figure 5. An example of a transient simulation that emulates the measurement of an analog material (Lunar). The simulated pressure (red and blue solid lines, for up- and downstream respectively) decreases to lower values than the measured pressure (dots), due to a slight performance deterioration of the vacuum pump.

with F_u and F_d determined by integrating the mass flux over the upstream and downstream boundary, respectively.

2.3.5. Meshing. Discretization is one of the most important aspects of an FEA, as it determines the computational cost and solution accuracy of a problem. Although the software is able to automatically generate a mesh based on the properties of the underlying physical model, manually defining a mesh can be advantageous when the nature of the solution is known. Thus, we chose the swept mesh method to utilize the symmetry of the problem, whereby a quadrilateral surface mesh is swept across the selected volume, creating a structured mesh of hexahedrons. From eight preset element size settings, the medium one was chosen as it builds a mesh of satisfactory resolution with a reasonable number of mesh elements.

For more complex studies, such as the analysis of wall layer effects in section 4.3 or sieve influence in section 4.4, the mesh settings had to be adapted. To provide a smooth solution in narrow domains or around sharp edges, it is necessary to improve the distribution and transition of element sizes.

3. Preliminary studies

3.1. Overview

In order to establish a baseline of simulation results that can be compared to the measurements, preliminary studies were performed with stationary and transient approaches. As described in section 2.3.4 the boundary conditions for the stationary simulations are less complicated than the transient counterpart. The terms with the partial time derivative become zero by definition, and the flux J is constant throughout the sample. So the downstream boundary condition (7) is replaced by the measured stationary pressure of the downstream compartment, whereas the upstream boundary condition is replaced by $J_u = J = \text{const}$. Under these conditions the pressure p throughout the sample is the unknown variable, for which the above discussed differential equations are solved for. Its value at the upstream surface, p_u, can be compared with the pressure measurement of the upstream compartment (see section 3.2). On the one hand, stationary simulations are useful to validate the measured pressure plateaus after the system came to stationary equilibrium, which provided the p_u, p_d and J values for the experimental determination of D^K and B. On the other hand, the whole process with transitions from one stationary plateau to the next cannot be analyzed in this way.

Therefore, also transient studies were performed, as they provide the possibility of comparing the dynamics of the system, such as the rate of pressure change. This includes the initial evacuation, followed by a number of fixed flow rate adjustments giving stationary pressures after sufficient setting time (used for evaluation to get D^K and B), and the respective transitions between them. An example for such a transient simulation is shown in figure 5, together with the corresponding measurement data of an analog material. For this purpose the upstream boundary condition (6) was implemented with the time-dependent flow rate F_{in} regulated by the gas flow controller, and the downstream boundary condition (7) with F_{out} calculated on the basis of the pump performance including the connecting hose.

3.2. Comparison with measurements

The preliminary studies were conducted with the measured parameter sets of 19 different samples. Eleven of them are composed of GB with a varying diameter range. Among

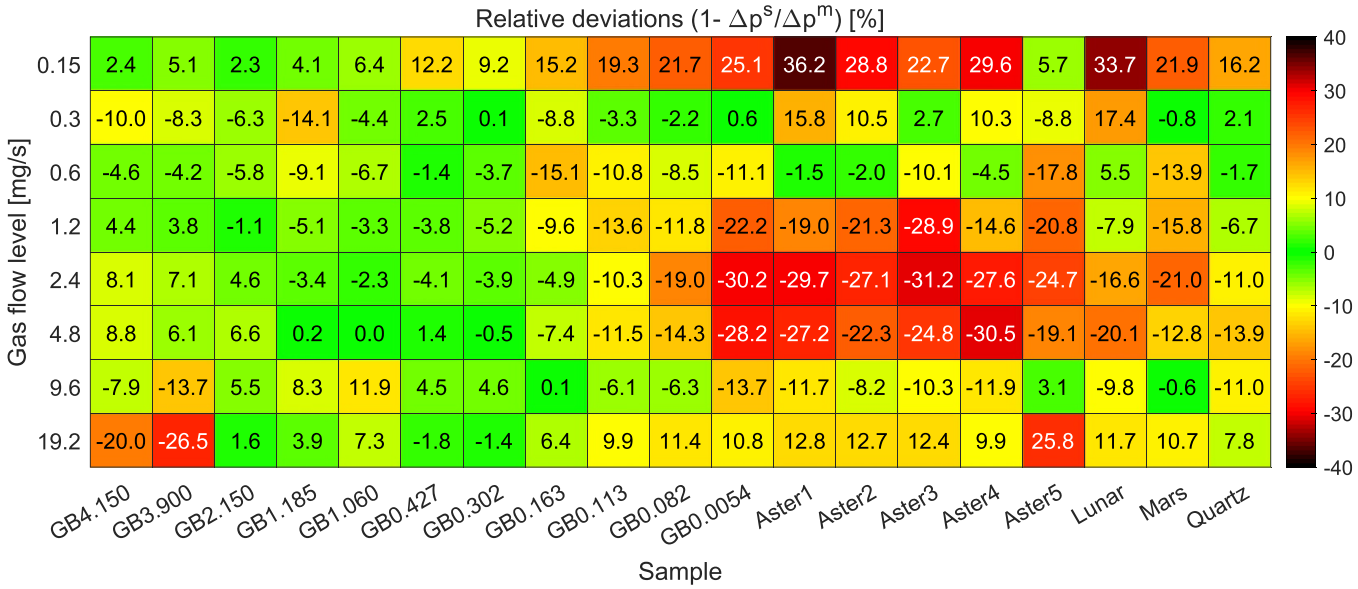

Figure 6. Relative differences between pressure drop results from measurements and stationary simulations, for each gas flow level and all measured samples.

the remaining samples, there are Martian and Lunar analogs, quartz sand, and five different packed samples of the same asteroid analog material. For measurements of high permeability samples, the transition between stationary conditions of different flow rates occurred in such short time periods that it could not be resolved with the applied measurement time cadence. In these cases, an accurate comparison of the dynamic process in the transition zones with the simulations was not possible. The comparisons of the steady-state from the transient simulations with the measurements, as well as with the results of the stationary simulations exhibited significant discrepancies. One of the main reasons for this was found to be an inaccurate description of the pump performance (due to degradation, the actual performance deviates from the nominal one given by the manufacturer). Anyway, the determination of B and D^{K} is only possible on the basis of stationary conditions with the respective pressure plateaus, which is why we mainly focus on the results of the stationary simulations in the following discussion.

Since for a given gas flux the material's flow parameters B and D^{K} directly correlate with the arising steady-state pressure difference across a sample (henceforth called 'pressure drop')

$$\Delta p = p_{\mathrm{u}}^{\sigma} - p_{\mathrm{d}}^{\sigma}, \tag{11}$$

it is the ideal quantity for comparing results from different methods. Hereby, the superscripts $\sigma \in \{\mathrm{m},\mathrm{s}\}$ denote whether the values are from measurements or stationary simulations, respectively. In the following figure 6 the relative deviation (given in percent)

$$\frac{\Delta p^{\mathrm{m}} - \Delta p^{\mathrm{s}}}{\Delta p^{\mathrm{m}}} \tag{12}$$

between the pressure drop in the sample as obtained by measurement and by stationary simulation is visualized. This comparison is best suited to assess how well the samples are characterized by the measured B and D^{K} values.

In these so-called heat maps (colored table plots) the rows list the applied external gas flux settings (in mg s^{-1}) and the columns the studied samples. There are several aspects to be noticed. Firstly, the measured pressure drop in all samples has positive as well as negative deviations from the theoretical stationary values obtained by simulation, whereby the sign depends on the applied gas flux. It gives evidence that the BFM with the determined B and D^{K} values does not represent the measured pressure-flux relation perfectly over the whole applied pressure range. The presence of positive as well as negative deviations stems from the fact that B and D^{K} were determined from the measurements by least square fits (Schweighart *et al* 2021), and so represent the behavior in an averaged fashion over the evaluated pressure range.

Among the GB samples, noticeably higher deviations are found for the largest and smallest size ranges. This is no surprise when taking into account the information given by Schweighart *et al* (2021): The beads above 4 mm diameter lead to extremely small pressure drop in the sample. The large pores occurring in these samples in relation to the overall sample size, provide very little resistance to the gas flow, so the pressure differences that develop across the sample may be smaller than the uncertainty of the pressure measurement. Consequently, the evaluation of these measurements for B and D^{K} is inaccurate. On the other side of the size range (below about 250 µm) the GB become increasingly non-spherical with decreasing size. The resulting surface roughness and angularity (in general, irregular shapes as a result of the manufacturing process) can cause an inhomogeneous distribution of grains over the sample. Such a high angularity

and variation in size is also typical for the grains of analog materials, which (at least partially) may explain the even more pronounced deviations of the measured pressure drop from the respective simulation. A more detailed discussion of this issue follows in section 4.1.

Another important factor that needs to be considered here is that all pressure plateaus measured for the largest two GB groups were above the respective Klinkenberg pressure (see figure 3), leading to less accurate results for D^{K}, even if the pressure drop is sufficiently high to allow an accurate subtraction of the up- and downstream pressure.

3.3. Parameter variations

One of the major advantages of numerical simulations over experiments is the precise control of individual parameters of the model. In particular, when some entities are inherently correlated and cannot be isolated, variation studies in simulations allow an assessment of the individual parameters' influence. For example by alternatively sweeping B and D^{K} through a range of values, while keeping the other constant, we could quantify the influence of each parameter in different regimes. Wider sweeps indicated, that the variation of either parameter has a greater effect when the constant counterpart is in the lowest range of the measured values (which corresponds to the respective values of the smallest grains, $B \sim 10^{-12}$ m^2 and $D^{\mathrm{K}} \sim 10^{-4}$ m^2·s^{-1}). This was to be expected since it means that the varied component of the flow (diffusive or viscous) is dominant. To quantify the effect of variations of either B or D^{K} on the pressure throughout the sample, we therefore kept the respective non-varied parameter at the mentioned minimum and swept the other over the range of the measurement uncertainty determined by Schweighart *et al* (2021). This analysis showed that the pressure deviations that arise due to the measurement uncertainties of B or D^{K} are below 1% for the steady-state. In contrast to this finding, the reproduction of the up- and downstream pressures by the simulations in section 3.2 yielded differences of up to about 30%, dependent on the gas flow level (figure 6). This gives evidence of the strength of the simultaneous evaluation of several measurements for pressure scenarios occurring at different flux levels, making the determination of B and D^{K} more stable and precise. However, also the downside of this technique becomes apparent, that is the averaging or even mimicking of effects which may change the pressure distribution but are not taken into account in the evaluation. These effects may be the local change of porosity and/or grain distribution within the sample, the pressure-dependent accuracy of the sensors or a temporal change of the sample during the measurement. The latter may result from the formation of cracks or channels in the sample, or from contraction with recession of the material from the container wall (such alterations have been observed typically in fine samples below 0.1 mm grain diameters). In the following section the importance of sample inhomogeneity and imperfect geometry is discussed in more detail.

4. Inhomogeneities and irregular sample geometry

To perfectly satisfy the assumption of homogeneity and isotropy, a sample needs to be very large compared to its characteristic length (determined by mean free path of molecules or average grain diameter). On the one hand, the properties of a finite sample can vary near the interfaces of the system boundary, depending on the setup. On the other hand, the sample preparation can introduce inhomogeneities inside. In the following, both aspects are analyzed. By comparing the simulation results for altered geometries or samples to those of the original preliminary studies, we ensure an isolated treatment of the effect of interest by adapting only the relevant parameters.

4.1. Porosity variation

According to equations (1) and (4), the steady-state is independent of ϵ. However, these equations do not consider the correlation between the flow parameters B, D^{K} and the porosity ϵ. Qualitatively, the more porous a medium is, the more permeable it is for gas flow. This relationship can be described analytically with simplifying assumptions about the pore space. For a packed bed of spheres, for example, the most common expression for the permeability as a function of porosity, is given by the Kozeny–Carman equation (Costa 2006)

$$B = C_{\mathrm{K\text{–}C}} \frac{\epsilon^3}{(1-\epsilon)^2}. \tag{13}$$

Here, $C_{\mathrm{K\text{–}C}}$ is a factor describing the pore structure. For a grain packing it depends on the size distribution and shape of the grains. To describe the dependency of D^{K} on porosity, Asaeda *et al* (1974) applied rigorous gas kinetic theory to gas molecule collisions with a packing of spheres. Similar results were already derived by Derjaguin (1994) using a different approach. Translated to our notation, the Derjaguin-Asaeda formula reads

$$D^{\mathrm{K}} = C_{\mathrm{D\text{-}A}} \frac{\epsilon^2}{1-\epsilon}, \tag{14}$$

where, in analogy to the above viscous case, $C_{\mathrm{D\text{-}A}}$ is a factor that depends on the geometry of the pores (or the spheres' diameters and an additional tortuosity factor which is of principal importance for non-spherical grains). In both descriptions, the proportionality factor is constant for a specific sample, as it only depends on the properties of the sample's individual particles when an isothermal process is assumed.

By implementing the definition of the flow parameters according to the equations above, simulations show that the pressure drop is rather sensitive to variations of the porosity of the whole sample. This can be made plausible by equation (10) from Schweighart *et al* (2021) (see also equation (16)), according to which the pressure drop Δp is indirectly proportional to $(\bar{p}B/\mu + D^{\mathrm{K}})$. Thereby, both B and D^{K} change considerably with ϵ in accordance with equations (13) and (14). For example, the variation of $\Delta\epsilon = \pm 0.1$ in a reference sample

with the parameters $B = 5 \times 10^{-11}\ \mathrm{m}^2$, $D^{\mathrm{K}} = 2 \times 10^{-3}\ \mathrm{m}^2\ \mathrm{s}^{-1}$ and $\epsilon = 0.4$ (similar to the parameters of GB in the size range 200–250 μm), increases or decreases the pressure drop roughly by a factor two respectively. Here it should be noted that in this simulation, the porosity of the whole sample was varied between individual cases but assumed spatially constant.

However, visual inspection of some prepared samples as well as the measurement of their porosities indicated that porosity variations also occur within individual samples, in particular as a function of the depth due to the Brazil nut effect. Therefore we also analyzed a scenario, where the porosity within one sample was varied by $\Delta\epsilon = 0.15$ along the cylinder axis (z) according to

$$\epsilon(z) = \bar{\epsilon}\left(1 - 0.075 + 0.15\frac{z}{L}\right), \tag{15}$$

where $\bar{\epsilon}$ is the average porosity. This was motivated by the porosity evaluation of many samples produced from the same material, showing variations of up to slightly above 10%. Therefore, we decided to use 15% as a maximum variation estimate. The parameters B and D_{K} were varied accordingly by inserting equation (15) in equations (13) and (14). This was performed for two sets of parameters, namely $\epsilon_0 \in \{0.4, 0.6\}$ and the corresponding average values for $B\,[\mathrm{m}^2] \in \{10^{-12}, 10^{-11}\}$ and $D_{\mathrm{K}}\,[\mathrm{m}^2\ \mathrm{s}^{-1}] \in \{3.2 \times 10^{-4}, 10^{-3}\}$. These values are typical for some of the analog materials (where porosity variations may be the result of the random pore structure changes due to the preparation process, or a consequence of the Brazil nut effect, which changes the grain size distribution). The simulated pressure drop resulting from this configuration (equation (15)) deviates less than one percent from the corresponding cases with the same average but constant porosity. Therefore we can conclude that a gradual linear change of porosity of up to 15% across a sample, according to equation (15), practically leads to the same measurement result as a sample with constant porosity $\bar{\epsilon}$.

Apart from gradual variations, also large-scale irregularities (relative to the grain size) of the porosity can occur in samples due to various reasons. Abrupt changes in pressure, for instance when the vacuum pump is activated, can create fissures or channels due to the sudden escaping of trapped air in the sample. This, as well as the fact that materials with rough, angular grains create irregular pore spaces due to interlocking mechanisms, was pointed out by Schweighart *et al* (2021). In addition to these inhomogeneities occurring already at the beginning of measurements, the experiment is further complicated by changes in the sample that can develop over the course of a measurement. For example the evaporation of minute moisture in some materials, and the consequent shrinking of the sample volume can also lead to cracks or gaps at the container wall. The main question at the root of this aspect is, how these irregularities in the sample contribute to the overall gas permeability and whether averaging over many of them makes sense. Since these inhomogeneities occur especially in analog samples and recent investigations by Skorov *et al* (2020, 2022) and Reshetnyk *et al* (2021, 2022) indicate their importance for the outgassing of cometary surfaces, it is crucial to control them in experiments. First, a careful procedure for the sample preparation, with appropriate use of a vibration table, facilitates the production of repeatable and homogeneous grain distributions. Second, a long evacuation period before the actual measurement starts, ensures that no moisture or other adsorbents are left in the vacuum chamber and the sample pores. Third, a very slow evacuation of the chamber can avoid abrupt pressure changes and minimize grain redistribution over the course of a measurement, in particular by a gas-flow triggered Brazil nut effect. To understand the sensitivity of gas flow measurements to irregularities (e.g. channels) despite these precautions, we performed corresponding calculations with simplifying assumptions, which are presented in the following sections.

4.2. Flow channels in the sample

The influence of a channel on the measurement of B and D^{K} can be analyzed on the basis of equation (10) from Schweighart *et al* (2021), which we write in the form

$$\Delta p\,\bar{p}\frac{A\,B}{\mu} + \Delta p\,A\,D^{\mathrm{K}} = -\frac{RTLF}{M} \tag{16}$$

with the pressure drop $\Delta p = p_{\mathrm{u}} - p_{\mathrm{d}}$ from one side to the other side of the sample of height L, and the mean pressure $\bar{p} = (p_{\mathrm{u}} + p_{\mathrm{d}})/2$. Provided that a channel of diameter d_{c} is present in the sample, which lies parallel to the axis of the cylindrical sample container, the total flow rate $F_{\mathrm{t}} = F_{\mathrm{s}} + F_{\mathrm{c}}$ is composed of the flow through the sample, F_{s}, and that through the channel, F_{c}. We assume that the channel is very thin compared to the sample diameter $d_{\mathrm{s}} \gg d_{\mathrm{c}}$, so that the influence of the gas moving through the channel has only negligible effect on the average flux through the sample. So equation (16) is applicable to both, the sample and the cylinder, whereby $(B, D^{\mathrm{K}}, F, A)$ are replaced with the actual specifications $(B_{\mathrm{s}}, D^{\mathrm{K}}_{\mathrm{s}}, F_{\mathrm{s}}, A_{\mathrm{s}})$ for the sample and $(B_{\mathrm{c}}, D^{\mathrm{K}}_{\mathrm{c}}, F_{\mathrm{c}}, A_{\mathrm{c}})$ for the channel, respectively. In the latter case, one has to substitute $B_{\mathrm{c}} = d_{\mathrm{c}}^2/32$, $D^{\mathrm{K}}_{\mathrm{c}} = d_{\mathrm{c}}\bar{c}/3$ and $A_{\mathrm{c}} = d_{\mathrm{c}}^2\pi/4$, obtaining a relation analogous to equation (10). This representation amounts to a parallel circuit of the two flow regions. The sum of the corresponding equations (16) can be brought into the same form, representing the total flow through the sample with channel, by defining an apparent permeability B_{app} and apparent Knudsen diffusion coefficient $D^{\mathrm{K}}_{\mathrm{app}}$,

$$\begin{aligned} B_{\mathrm{app}} &= (B_{\mathrm{s}}A_{\mathrm{s}} + B_{\mathrm{c}}A_{\mathrm{c}})/A, \\ D^{\mathrm{K}}_{\mathrm{app}} &= (D^{\mathrm{K}}_{\mathrm{s}}A_{\mathrm{s}} + D^{\mathrm{K}}_{\mathrm{c}}A_{\mathrm{c}})/A, \end{aligned} \tag{17}$$

where $A = A_{\mathrm{s}} + A_{\mathrm{c}}$ is the total cross section through the porous medium including the channel. Thus, the total flow rate satisfies the equation

$$\Delta p\,\bar{p}\frac{A\,B_{\mathrm{app}}}{\mu} + \Delta p\,A\,D^{\mathrm{K}}_{\mathrm{app}} = -\frac{RTLF_{\mathrm{t}}}{M}. \tag{18}$$

The analogy with equation (16) proves that the evaluation of the measurements for the permeability and Knudsen

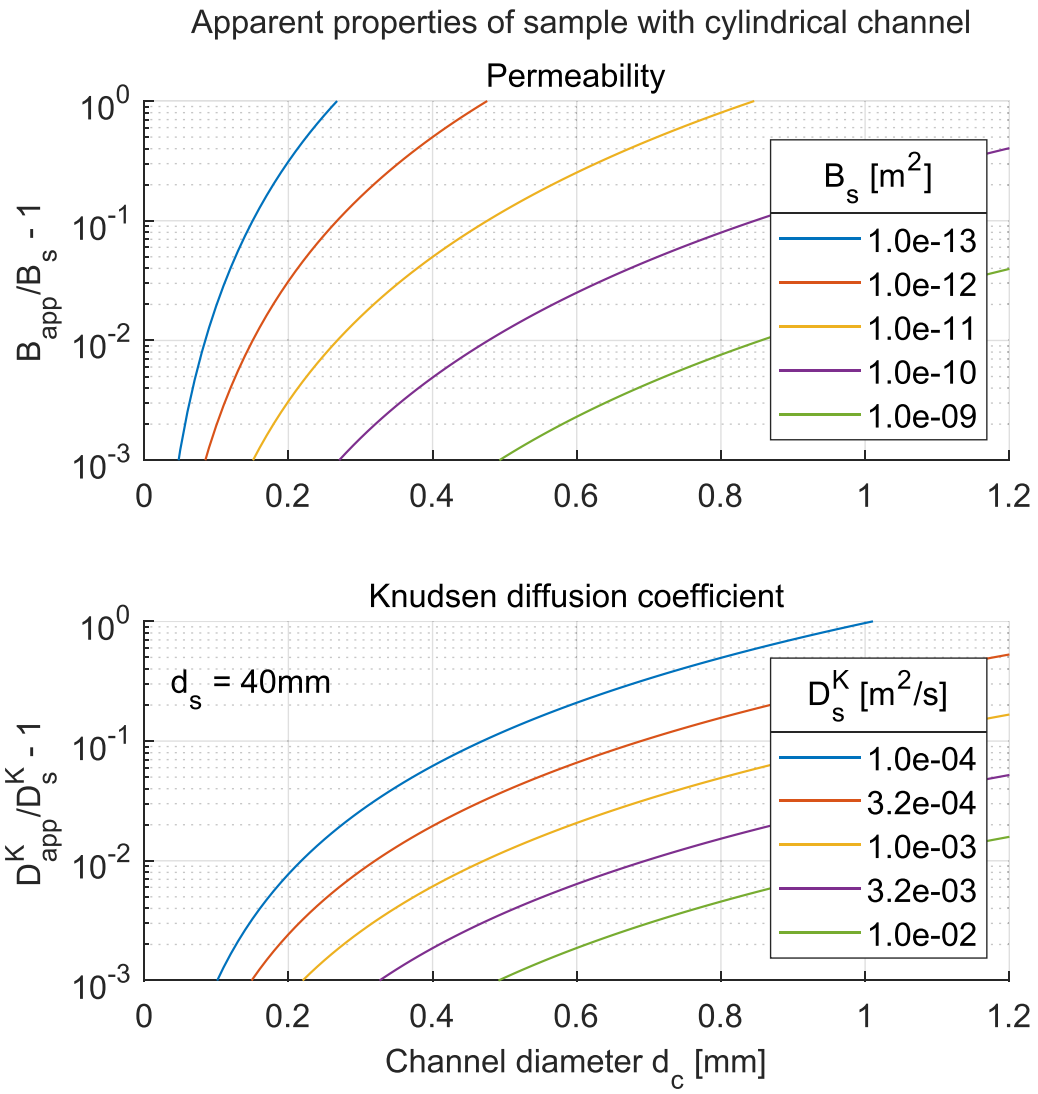

Figure 7. Apparent viscous permeability B_{app} and Knudsen diffusion coefficient D^K_{app} as measured when a channel is present in the sample parallel to the net gas flow direction. The shown quantities are relative deviations from the respective true parameters of the sample material, B_s and D^K_s, respectively. For instance, the value 0.01 (or 1) on the ordinate means that the corresponding channel flow contributes about 1% of (or the same as) the respective sample flow.

diffusion coefficient actually yields the apparent quantities (equation (17)) instead of the ones for the porous medium itself. The relative deviations $(B_{app} - B_s)/B_s$ and $(D^K_{app} - D^K_s)/D^K_s$ as caused by the channel depend on its diameter. Figure 7 visualizes this error for different media, measured in a cylindrical container of inner diameter $d_s = 40$ mm. The examples used for B_s and D^K_s span a range containing typical comet analog materials and GB with diameters from about 0.01 to 1 mm (compare figure 1). Corresponding colors in the upper and lower panel of figure 7 roughly refer to the same medium and the shown ordinates span the same grain sizes, which follows from the dependence of B and D^K on d_g^2 and d_g, respectively. This is in accordance with the Kozeny–Carman and Derjaguin-Asaeda equations as well as with the measurements shown in figure 1.

For the regarded media, the effect of the channel is practically negligible if it is thinner than 0.1 mm. For such thin channels the Knudsen diffusion prevails and the error in B is irrelevant. For thicker channels, there is generally a more pronounced effect on B than on D^K. Channels can make a determination of the sought parameters unfeasible if the grains of the packing are too small. For example, a packing with an abundance of grains of tens of micrometers in diameter (typical analog materials are of this category) are found in the plots of figure 7 above the red curves. So 0.3 mm channels lead to errors in B of about 20%, but D^K is still accurately measurable. In contrast to that, for GB of 1 mm diameter (or larger), even a channel of the same diameter has no important influence on the measurement of either of the two parameters.

4.3. Boundary effects

Describing a finite granular sample with one set of parameters is virtually equivalent to cutting out a part from an infinite medium, where on average the grains are distributed uniformly. However, in reality the granular material is filled into

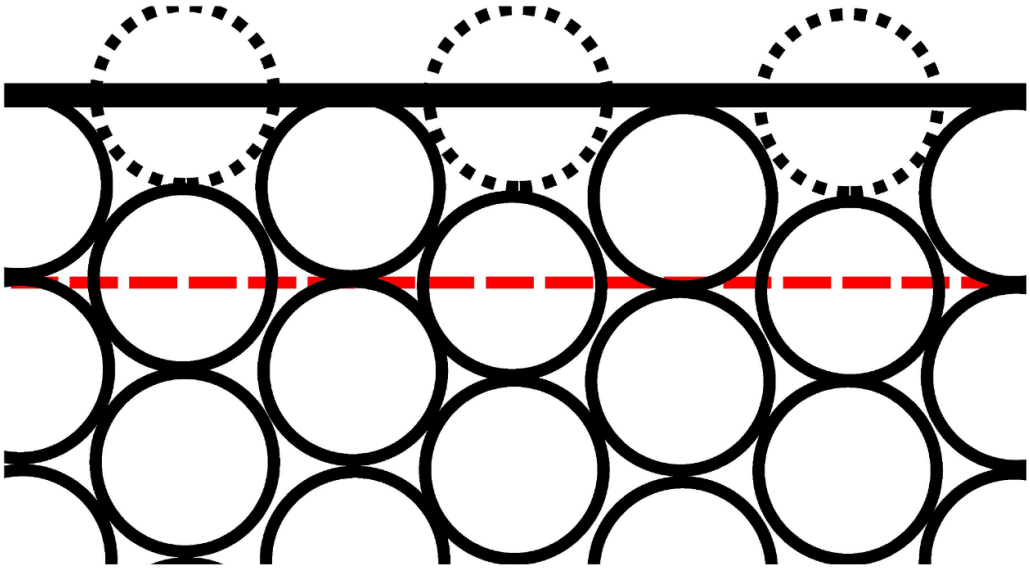

Figure 8. Visualization of the effect of increased porosity that arises in a layer at the sample surface (above red dashed line) along the container boundary (thick black line). In the case of a sample cutout from an extended medium, parts of the dashed grains would fill the empty spaces.

a container, whereby the grains can only have contact points with the container wall, in contrast to the virtual case, where cross sections of the grains build part of the container wall as illustrated in figure 8. The real wall vicinity is a grain depletion zone, where fewer grains are present in a layer of about a grain diameter thickness (henceforth referred to as 'wall layer'), than in the virtual cutout from a larger medium. To assess this effect in view of the gas flow through GB, we first estimated that the volume filling factor $v_f = 1 - \epsilon$ would decrease by 30% in the wall layer (further justification below). For the majority of GB samples, this corresponds to a change of porosity from $\epsilon \approx 0.35$ to $\epsilon \approx 0.54$ and for the more porous samples from $\epsilon \approx 0.54$ to $\epsilon \approx 0.68$. To analyze the influence of this wall layer, we adapted the preliminary studies for three sets of parameters to represent a coarse ($d_g = 3.8$ mm), medium ($d_g = 250\,\mu$m) and fine ($d_g = 63\,\mu$m) sample. The thickness of the wall layer was set to the respective grain diameter, and the flow parameters B and D^K within this thin region were scaled according to equations (13) and (14). A quantity well suited for comparison with the preliminary studies, is again the steady-state pressure drop across the sample (difference between upstream and downstream pressure plateaus), as it is a measure of the resistance of the sample to the gas flow. Table 1 summarizes the relative changes of the pressure drop that occur in samples with an adapted wall layer as compared to the respective homogeneous samples. The rows refer to the investigated thicknesses of the wall layer (equal to grain size d_g) and the columns indicate the change of porosity. The greatest effect is obtained for the porosity change from $\Delta\epsilon =$ 0.35 to 0.54 with the largest GB, where the wall depletion zone decreases the steady-state pressure drop by 68%–59%, depending on the gas flow level. As mentioned in section 2.3.5, the mesh settings had to be adapted for this study to guarantee a smooth solution across the wall layer and the interface to the bulk sample. This was achieved by manually defining

Table 1. Relative change of the pressure drop in percent, caused by a wall layer of higher porosity.

	Porosity change: $\epsilon_{bulk} \longrightarrow \epsilon_{wall}$	
Wall layer thickness	$0.35 \longrightarrow 0.54$	$0.54 \longrightarrow 0.68$
$d_g = 3.8$ mm	-68 to -59	-52 to -47
$d_g = 250\,\mu$m	-9 to -6	-6 to -3
$d_g = 63\,\mu$m	-2 to -1.2	-1

the number of mesh nodes along each interface (sample surfaces and wall layer-bulk boundary). Due to the larger number and smaller size of the mesh elements, particularly for the fine sample, some computations took excessive time. To limit the use of resources without compromising the resolution of the solution, we exploited the cylinder symmetric nature of this problem.

To verify the estimation of the wall layer porosity, a virtual sample was created using *LIGGGHTS*® (see figure 9). This open source software is commonly used to simulate granular material with the discrete element method (DEM) (Kloss and Goniva 2011, Desu *et al* 2018). In this context it was used to simulate the filling of a cylindrical container (ballistic deposition) with a predefined number of uniform spherical particles. Next, the cylinder was formally divided into concentric, circular rings (hollow cylinders), each with the width of one sphere diameter. Subsequently, the positions of all spheres, which were obtained from the DEM simulation, were sorted radially. If a sphere stretched across two segments, its exact volume fractions belonging to the respective segments were computed analytically. Thus, the total volume occupied by spheres could be given separately for each ring segment, enabling the calculation of a radially discretized porosity distribution. This is plotted for a virtual sample of monodisperse spheres in figure 10 (0.5 mm sphere diameter, 47.61 mm

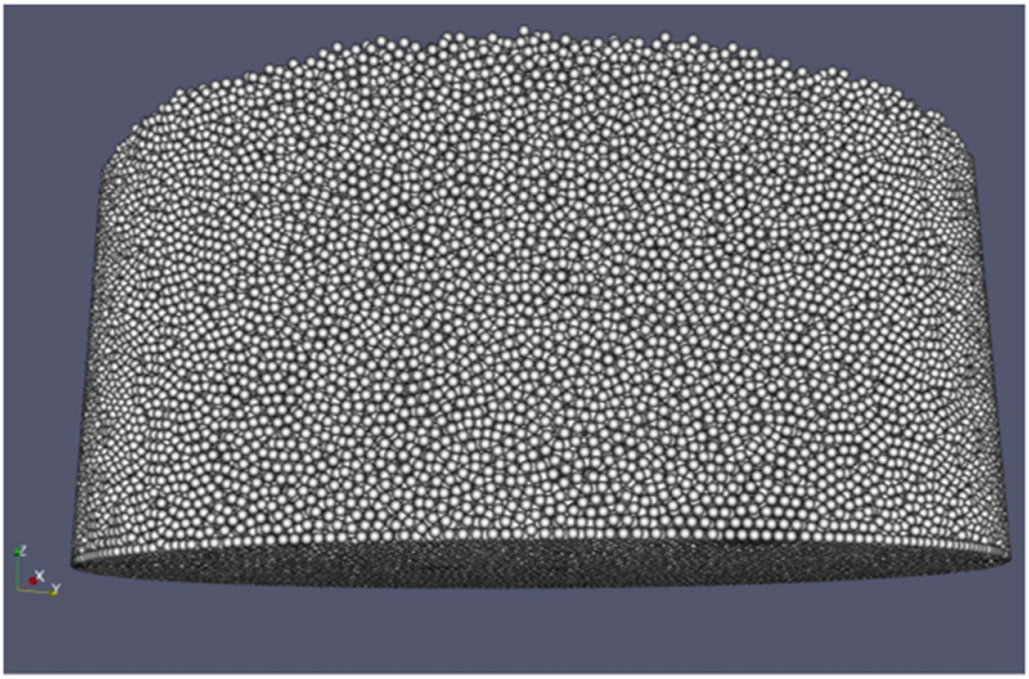

Figure 9. Ballistic deposition packing of monodisperse spheres (0.5 mm diameter) created with the LIGGGHTS software.

container diameter and 11.76 mm sample height). The average porosity of roughly 0.37 in the bulk sample is very close to the measured porosities of the real samples. The most important result of this calculation is the jump of porosity in the outermost segment, which even extends to the second layer from the boundary. As it is lower than the estimate used in the simulations, the values provided in table 1 represent an upper limit for this boundary effect. It has to be emphasized that these considerations are based on a monodisperse packing, and that the effect for polydisperse cases would crucially depend on the grain size distribution.

4.4. Geometric features

As described in section 2, the evaluation of the measurements and the simulations of the preliminary studies were carried out with the assumption, that the sample material has the form of a cylinder with a flat base. In reality however, the experimental setup comprises additional geometric features such as the sieve. The simulation results of the following analyses are again compared with the results of the ideal geometry of the preliminary studies.

The presence of the sieve can affect the gas flow through the sample in two ways. On the one hand, the sieve wire grid that holds the sample, is an additional obstacle in the path of the gas molecules and can be regarded as a layer of porous structure itself. On the other hand the meshes of the sieve grid may be plugged by grains which are only slightly bigger, leading to a choking effect. Although the former effect of a standalone sieve was tested by Schweighart *et al* (2021) and no influence could be detected even for the finest sieve, it should be noted that those tests were performed without any sample. To check if there is any interaction between the sieve's grid and the sample's particles (e.g. particles settling in the sieve holes), the experiment would have to be repeated with a sample but without a sieve. As this is not possible experimentally, we analyzed this aspect with simulations based on the following coarse estimates. The sieve mesh is described as a wire grid with a square pattern, where the width of the holes match the diameter of the spherical particles d_g. Albeit a very unlikely case, this leads to maximum choking and so to an estimate of the maximum influence of the sieve, where each hole of the sieve is filled with a particle. This would result in a situation where every particle is surrounded by 4 pores inside a single grid mesh, each with the area A_p and perimeter P_p as shown in figure 11. Also here, the total gas flux through the pores consists of a viscous bulk flow component and a contribution due to the effusion of gas molecules through the aperture. A description for the former, in the limit of infinitely thin circular pores, is given by the Sampson flow (Sampson and Greenhill 1891, Heiranian *et al* 2020)

$$J_\mathrm{Sampson} = \frac{(p_2 - p_1) d_\mathrm{p} \bar{p}}{6\mu\pi RT}, \tag{19}$$

where p_2 and p_1 are the pressures on either side of the pore (with $p_1 + p_2 = 2\bar{p}$), d_p the diameter of the circular aperture and J_Sampson the average viscous flux through it. As the validity of this formula also extends to very thin pores according to Weissberg (1962), we apply it as a first approximation in our case of non-circular pores. To roughly account for the fact, that the pores around the particles are not circular, their diameter is expressed as a ratio of the area A_p to the perimeter P_p:

$$d_\mathrm{p} = \frac{4A_p}{P_\mathrm{p}} = \frac{d_\mathrm{g}^2 - \frac{d_\mathrm{g}^2\pi}{4}}{d_\mathrm{g} + \frac{d_\mathrm{g}\pi}{4}} = d_\mathrm{g}\frac{4-\pi}{4+\pi}. \tag{20}$$

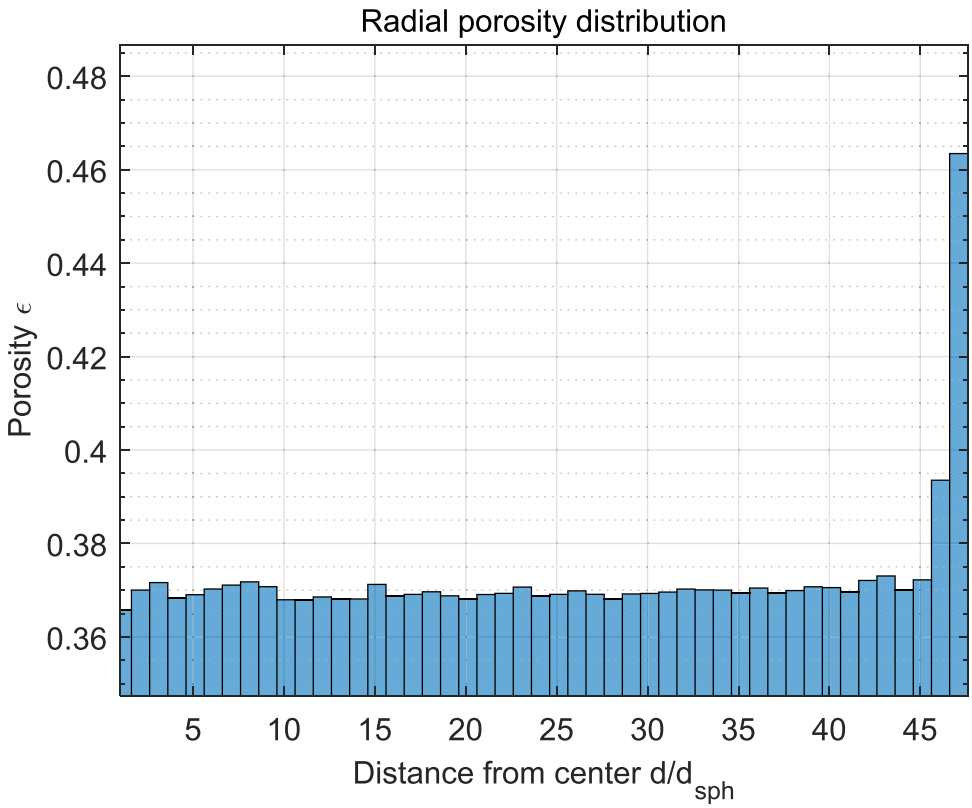

Figure 10. Radial porosity distribution of the sample shown in figure 9. The bins represent hollow cylinders with the thickness of one sphere diameter (except for the first bin) and the abscissa counts the distance from the center of the cylinder in the same unit (0.5 mm).

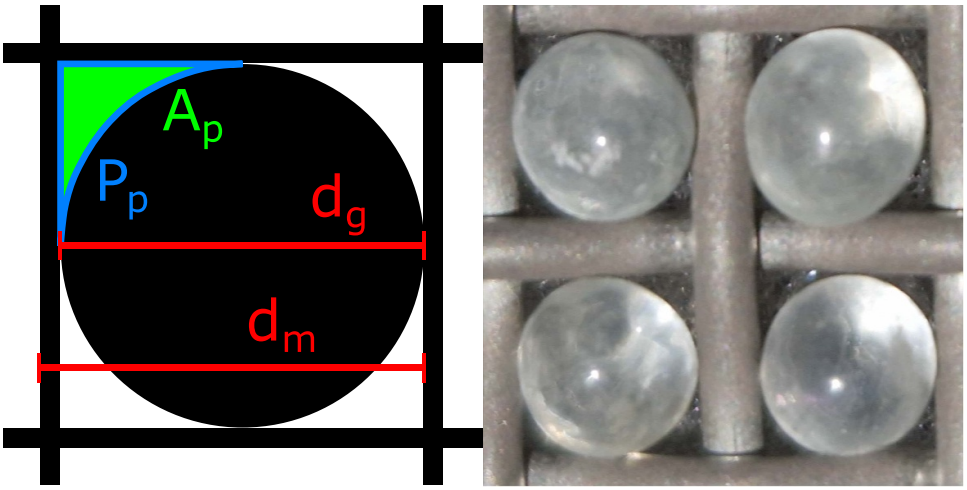

Figure 11. Left: schematic drawing of a situation where the holes of a sieve are filled by particles, resulting in 4 pores around every particle, each with an area A_p and perimeter P_p. Right: a real sieve, with glass beads plugging the holes.

To describe the effect of effusion (diffusive Knudsen flux through the aperture), an isotropic Maxwell distribution is assumed for the gas molecules on both sides of the pore. The molecular flux J_1 through the pore from one side is then proportional to half the average particle velocity ($\bar{v} = \sqrt{8RT/(\pi M)}$) times half the gas density. This part of the Hertz relation (Persad and Ward 2016) is the result of the integration over all incidence angles of the particles moving in the respective direction. As the same holds true for the flux J_2 from the other side (except for the sign), the total effusive flux J_eff is given by the sum:

$$J_\mathrm{eff} = J_2 - J_1 = \frac{\bar{v}}{2} \cdot \frac{n_2 - n_1}{2} = \frac{\bar{v}}{4RT}(p_2 - p_1). \qquad (21)$$

Taking into account that the average flux through the whole sample cross section A is smaller by a factor $4A_\mathrm{p}/d_m^2$ than the flux through the pores left between a sieve mesh of width d_m

Table 2. Range of relative deviations of pressure drop Δp caused by the sieve wire grid.

d_g (mm)	t_{sieve} (mm)	Δp change (%)
4	1	5.9–18.4
1	0.3	2.0–3.2
0.5	0.2	0.9–1.1
0.05	0.035	0.2–0.5

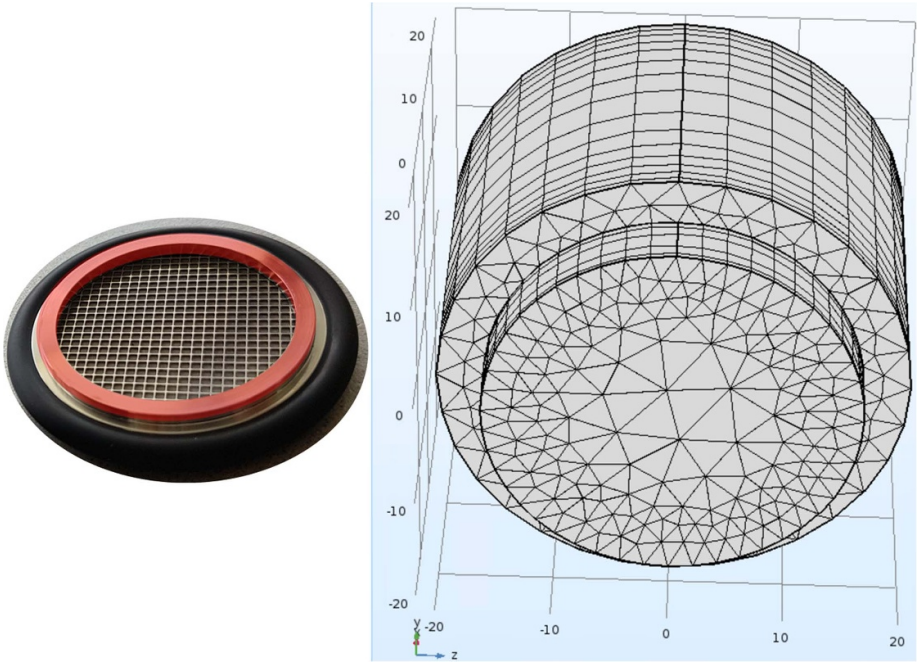

Figure 12. Left: the ring highlighted in red and intended to center the sieve when mounted on the sample container, protrudes into the sample in the lowest 5 mm and thus reduces the cross sectional area of the gas flow. Right: the constriction is implemented in the simulation by adapting the geometry of the model.

(grading plus grid wire thickness) and the grain (green area in figure 11), the sum of the viscous and effusive flux, averaged over the whole cross section, reads

$$J = \frac{p_2 - p_1}{RT}\left(\frac{\bar{v}}{4} + \frac{\bar{p} d_g}{6\mu\pi}\frac{4-\pi}{4+\pi}\right)\frac{4A_p}{d_m^2}. \tag{22}$$

Comparing the resulting total flux with equation (10) from Schweighart *et al* (2021) proves that the flow rate penetrating the sieve is equal to the flow through a porous thin layer with flow parameters

$$\begin{aligned} B_{sieve} &= \frac{4-\pi}{4+\pi}\frac{d_g t_{sieve}}{6\pi}\frac{4A_p}{d_m^2}, \\ D_{sieve} &= \frac{\bar{v} t_{sieve}}{4}\frac{4A_p}{d_m^2}. \end{aligned} \tag{23}$$

Hereby, t_{sieve} is the thickness of the surrogate sieve for the implementation in the simulations. The latter was added as a layer of thickness t_{sieve} to the bottom face of the sample cylinder, setting the flow parameters in this layer according to equation (23). To analyze different cases, various values for d_g and t_{sieve} were simulated, using standard values for the applied sieve wire thickness as available (see Riffert *et al* 2022) for the needed respective grading (which must be smaller than the grain size, but large enough to be sufficiently robust). Table 2 summarizes the corresponding parameters of the sieve and the respective calculated pressure effect for comparison. Considering that the difference between the bulk and sieve parameters is not extreme, and that the sieve grid is very thin compared to the sample height, it is plausible that, except for the largest beads, the steady-state results of these simulations show no considerable effect of the sieve. However, for the largest 4 mm beads the influence is severe, since only about ten bead layers on top of each other build the sample, and so their resistance to gas flow is so small that the resistance of the choked sieve meshes are significant in comparison. The consequence is that the sieve holding the larger bead fractions should always be of a grading much smaller than the beads size. This is only possible when the mesh is additionally supported by a coarse grid so that the fine wire grid does not bend or break under the load (and gas flow drag). This solution was also applied by Schweighart *et al* (2021). From the above findings and from measurements we know that this coarse grid support has no relevant influence on the measurements. The second way that the sieve can impede the gas flow, is related to its mechanical design. To mount the sieve at the bottom of the sample container, a ring protrudes from the main contact plane of the sample and mesh grid (see figure 12 left image). This ring

Table 3. Range of relative deviations of the steady-state pressure gradients between simulations with and without a constricting sieve ring.

	Relative deviations (%)		
Constricted diameter (mm)	Coarse sample	Medium sample	Fine sample
36	6.7–7.2	5.0–5.9	3.8–5.1
32	16.2–17.6	12.2–15.1	9.6–13.5

causes a constriction of the cross sectional area of the gas flow in the lowest 5 mm of the sample. For one type of sieve, the diameter is reduced from 40 mm to 36 mm and for another type it is even reduced to 32 mm, which translates to a reduction of the cross-sectional flow area by 19% and 36%, respectively. To understand how this constraint affects the overall pressure evolution of a sample, the geometry of the initial simulation model of the preliminary studies was adapted (see figure 12 right image). Counting 5 mm from the downstream sample surface along the cylinder axis, the diameter was reduced by 4 mm or 8 mm, respectively. For each of these cases, three different types of samples were simulated, representing a coarse (GB 4.0–3.8 mm), medium (GB 355–250 µm) and fine (GB 100–63 µm) grain size distribution. Also in this study, the quantity best suited for comparison is the steady-state pressure drop. Hence, the deviations of the latter relative to the corresponding steady-state results of the preliminary studies without a sieve ring are summarized in table 3. As the pressure plateaus of different gas flow levels were computed, the ranges are given in which the deviations lie. The simulations reveal that it is important to reduce the ring constriction as much as possible. While the thin ring is acceptable for fine grains, it causes changes of the pressure drop of more than 5% for beads larger than about 1/100 the sample container dimension. The thick ring reduces the measurement accuracy by 10%–20%. Therefore a different kind of sieve support will be used for future measurements with no or at least thinner constriction of the sieve grid mounting.

5. Conclusions

The viscous permeability B and Knudsen diffusion coefficient D^{K} are used to describe the gas flow through porous media on the basis of the BFM. In this work we analyzed the effect of certain systematic errors of B and D^{K} not addressed previously but typically occurring in laboratory experiments across a broad pressure regime. By using the measured parameters along with other quantities determining the gas flow process (temperature, flow rate, sample porosity) as input for our simulations, we computed the pressure distributions in different samples. A comparison of the simulated pressures with the actually measured ones enabled the validation and estimation of the accuracy of the measurements. The FEM based solver COMSOL proved to be a suitable tool, with which the underlying differential equations and boundary conditions could be implemented appropriately.

Our analysis focused on experiments recently performed for GB and cometary and planetary analog materials by Schweighart *et al* (2021). They already studied the occurring random errors and identified some important sources of bias, but did not address systematic errors caused by the sample support sieve, the effect of the sample container wall and of non-homogeneous regions in the sample (which may develop during the measurements). Transient as well as stationary flow computations were made, where the former served mainly for a check of the experimental setup (e.g. to verify the pump performance). The main results are for the stationary flow since they are used to determine the sought parameters B and D^{K}.

First preliminary simulations verified (Schweighart *et al* 2021) in their conclusion that the measurement of the largest GB fraction (diameter 4 mm) is most error-prone due to insufficient pressure differences across the samples. Further, the simulations of the smallest groups (0.1 mm and below) confirm that the grains are not fully symmetrical anymore, leading to higher tortuosity. This effect is even stronger for very angular grains, which also explains the deviations between simulations and measurements in the case of the analog materials.

The sample is supported by a sieve composed of a mounting ring and a fine mesh, the influence of which was checked by reference measurements without any sample. No influence could be detected (negligible pressure drop was caused by the sieve). However, the interaction of the sample with the sieve could not be analyzed experimentally. Therefore we simulated the full configuration (sample with sieve) for different application cases, i.e. various mounting rings causing different constrictions of the flow, as well as different mesh gradings, as needed for the respective sample grains. The analytic estimation of the maximum possible resistance of the sieve mesh confirmed its influence to be negligible (except for the largest GB, where other errors are more prominent). In contrast to that, the constriction of the flow area by the sieve's mounting ring can lead to noticeably higher pressure gradients. Based on these findings, we recommend the use of a sieve with minimal flow constriction (less than the average grain diameter) and a mesh grading that is much finer than the grains of a sample. An additional coarse wire grid beneath the fine mesh (as used by Schweighart *et al* 2021) provides the mechanical stability for holding the sample without deflection.

Even if grains are distributed uniformly throughout a sample, a slight depletion of the grain density occurs near the walls of the sample container, creating a wall layer with a porosity different from that of the inner sample. Based on an exemplary virtual packing of monodisperse spheres created with the DEM, we found for an average sample porosity of about 0.37, an increase by $\Delta\epsilon \approx 0.1$ in a wall layer of one grain diameter thickness. We performed the gas flow simulations assuming a slightly larger jump in porosity to obtain an estimate of the maximum wall layer effect. The results show a dramatic effect when the grain size is about a tenth of the container dimension. For an accurate measurement of B and D^{K}, a container of at least 100 grains in diameter is recommended.

Though the effects of the sieve and wall layer can occur simultaneously and even compensate each other partially (see tables 1 and 3), we analyzed them separately. The primary reason for this was to understand the individual impact of each,

also in view of future applications in realistic environments. Both effects may be found in comet surface materials if large pebbles are present. The occurrence of general porosity variations on the comet 67P Churyumov–Gerasimenko, as well as their influence on various physical processes (i.e. gas flow and heat transport), has been elaborated by several authors Spohn *et al* (2015), Lethuillier *et al* (2016), Christou *et al* (2018), Reshetnyk *et al* (2022), Skorov *et al* (2022). In any case, our calculations not only prove the significance of these effects in laboratory experiments for the measurement of B and D^{K}. They also contribute to the general understanding of how an additional fine layer can affect the overall gas flow through granular material. The situation of the sieve analysis, with the geometry turned upside down, may also occur on a comet surface when a thin layer of fine dust may be present in virtue of dust precipitation (Thomas *et al* 2015).

In addition to the effects summarized above, we analyzed cylindrical channels that sometimes manifest themselves in fine grain samples during a measurement campaign. Channels usually arise in a non-uniform way, leaving a non-circular, sometimes ramified, structure of varying thickness. Nevertheless our simplified approach using a straight circular tube in net flow direction gives a rough estimate of the order of its effect on the gas flow. Our analysis implies that the influence on the measured (apparent) B and D^{K} values are negligible if the channels are less than 0.1 mm in diameter. They have more influence if the channels get thicker and the sample is more resistant to gas flow. For $D^{\mathrm{K}} \approx 10^{-3}\ \mathrm{m^2\ s^{-1}}$ or smaller, which holds for most analog materials, a channel of 0.5 mm thickness leads to an error of at least 1%, reaching about 4% for $D^{\mathrm{K}} \approx 3 \times 10^{-4}\ \mathrm{m^2\ s^{-1}}$. The permeability B is much more sensitive to channel influences, but plays only a role for analog materials at pressures above about 10^3 Pa, since their Klinkenberg pressure is above 10^4 Pa.

In summary, the simulations presented in this paper proved to be a valuable assessment of accuracy aspects of the gas flow experiments for determining the flow characteristics of porous media, as performed recently in the context of cometary analog materials. It has improved our understanding of effects of the setup on the measurement quality and thus enables us to pinpoint open issues for future research activities. Among these are the important questions of the preparation of samples and their alteration during the measurement. In particular, erosion and generally the building of cavities, like channels or cracks, inside the sample and at the container wall, belong to the most challenging effects. Also the variation of the grain distribution and consequently of the porosity, caused by an uneven settling of angular grains or by the Brazil nut effect, can change the gas flow characteristics considerably.

Finally, it has to be emphasized that the gas flow properties crucially depend on the shape of the grains. Angular grains lead to more complicated packing and pore structures. Shape descriptors like elongation, sphericity, convexity and fractal dimension that are used for particle classification of dust in space science (Kim *et al* 2022), may also yield valuable clues on the effect of grain shape on the gas flow through packed beds. Whether this would render a quantitative approach to angularity, which correlates with porosity and characteristics of gas flow through the medium, is therefore a topic recommended for future studies.

Data availability statement

The data that support the findings of this study are available upon reasonable request from the authors.

Acknowledgments

This research was carried out in the framework of the CoPhyLab project, funded in part by the Austrian Science Fund (FWF) through the D-A-CH programme (GU 1620/3-1 and BL 298/26-1/SNF 200021E 177964/FWF I 3730-N36). For the purpose of open access, the author has applied a CC-BY public copyright license to any author accepted manuscript version arising from this submission.

ORCID iDs

Sunny Laddha https://orcid.org/0000-0003-3628-5450
Wolfgang Macher https://orcid.org/0000-0002-2683-5060
Günter Kargl https://orcid.org/0000-0001-9125-0256

References

Asaeda M, Yoneda S and Toei R 1974 Flow of rarefied gases through packed beds of particles *J. Chem. Eng. Japan* **7** 93–98
ASTM E11 2017 Specification for woven wire test sieve cloth and test sieves (available at: www.astm.org/e0011-17.html)
Barucci M A and Fulchignoni M 2017 Major achievements of the Rosetta mission in connection with the origin of the solar system *Astron. Astrophys. Rev.* **25** 3
Benkhoff J and Spohn T 1991 Results of a coupled heat and mass transfer model applied to KOSI sublimation experiments *Theoretical Modelling of Comet Simulation Experiments* ed N Kömle, S Bauer and T Spohn (Vienna: Austrian Academy of Sciences Press)
Bischoff D, Gundlach B, Neuhaus M and Blum J 2019 Experiments on cometary activity: ejection of dust aggregates from a sublimating water-ice surface *Mon. Not. R. Astron. Soc.* **483** 1202–10
Bland P A, Cressey G and Menzies O N 2004 Modal mineralogy of carbonaceous chondrites by x-ray diffraction and Mössbauer spectroscopy *Meteorit. Planet. Sci.* **39** 3–16
Britt D T, Cannon K M, Donaldson Hanna K, Hogancamp J, Poch O, Beck P, Martin D, Escrig J, Bonal L and Metzger P T 2019 Simulated asteroid materials based on carbonaceous chondrite mineralogies *Meteorit. Planet. Sci.* **54** 2067–82
Chen J, Hou J, Wang R and Hui Y 2017 The effect of Knudsen diffusion and adsorption on shale transport in nanopores *Adv. Mech. Eng.* **9** 168781401772185
Christou C, Dadzie S K, Marschall R and Thomas N 2020 Porosity gradients as a means of driving lateral flows at cometary surfaces *Planet. Space Sci.* **180** 104752
Christou C, Dadzie S K, Thomas N, Marschall R, Hartogh P, Jorda L, Kührt E, Wright I and Rodrigo R 2018 Gas flow in near surface comet like porous structures: application to 67P/Churyumov-Gerasimenko *Planet. Space Sci.* **161** 57–67
Costa A 2006 Permeability-porosity relationship: a reexamination of the Kozeny-Carman equation based on a fractal pore-space geometry assumption *Geophys. Res. Lett.* **33** L02318

Derjaguin B 1994 Measurement of the specific surface of porous and disperse bodies according to the resistance offered to the flow of rarefied gases *Prog. Surf. Sci.* **45** 337–40
Desu R K, Moorthy A and Annabattula R K 2018 Dem simulation of packing mono-sized pebbles into prismatic containers through different filling strategies *Fusion Eng. Des.* **127** 259–66
Grün E, Benkhoff J and Gebhard J 1992 Past, present and future KOSI comet simulation experiments *Ann. Geophys.* **10** 190–7
Grün E *et al* 1991 Laboratory simulation of cometary processes: results from first KOSI experiments *IAU Colloq. 116: Comets in the Post-Halley Era* (*Astrophysics and Space Science Library* vol 167) ed R L J Newburn, M Neugebauer and J Rahe pp 277–97
Gundlach B, Fulle M and Blum J 2020 On the activity of comets: understanding the gas and dust emission from comet 67/Churyumov–Gerasimenko's south-pole region during perihelion *Mon. Not. R. Astron. Soc.* **493** 3690–715
Gundlach B, Schmidt K P, Kreuzig C, Bischoff D, Rezaei F, Kothe S, Blum J, Grzesik B and Stoll E 2018 The tensile strength of ice and dust aggregates and its dependence on particle properties *Mon. Not. R. Astron. Soc.* **479** 1273–7
Gundlach B, Skorov Y and Blum J 2011 Outgassing of icy bodies in the solar system—I. The sublimation of hexagonal water ice through dust layers *Icarus* **213** 710–9
Haack D 2022 Experimental simulation for the analysis of geomorphological properties of cometary surfaces with volatile outgassing *PhD Thesis* Freie Universität Berlin
Haack D, Lethuillier A, Kreuzig C, Feller C, Gundlach B, Pommerol A, Blum J and Otto K 2021 Sublimation of ice-dust mixtures in cooled vacuum environments to reproduce cometary morphologies *Astron. Astrophys.* **649** A35
Haack D, Otto K, Gundlach B, Kreuzig C, Bischoff D, Kührt E and Blum J 2020 Tensile strength of dust-ice mixtures and their relevance as cometary analog material *Astron. Astrophys.* **642** A218
Heiranian M, Taqieddin A and Aluru N R 2020 Revisiting Sampson's theory for hydrodynamic transport in ultrathin nanopores *Phys. Rev. Res.* **2** 043153
ISO 3310-1:2016 2016 *Technical Requirements and Testing—Part 1: Test Sieves of Metal Wire Cloth* (International Organisation for Standardization) (available at: www.iso.org/standard/62410.html)
ISO/IEC Guide 98-3:2008 2010 *Uncertainty of Measurement* (International Organisation for Standardization) (available at: www.iso.org/standard/50461.html)
Kast W and Hohenthanner C-R 2000 Mass transfer within the gas-phase of porous media *Int. J. Heat Mass Transfer* **43** 807–23
Kim M, Mannel T, Lasue J, Longobardo A, Bentley M and Moissl R 2022 Primitiveness of cometary dust collected by MIDAS on-board Rosetta *EGU General Assembly 2022 (Vienna)*
Klinkenberg L 1941 The permeability of porous media to liquids and gases *Proc. OilGasScientificResearchProjects Institute, SOCAR* pp 57–73
Kloss C and Goniva C 2011 *Liggghts—Open Source Discrete Element Simulations of Granular Materials Based on Lammps* (New York: Wiley) pp 781–8
Kreuzig C *et al* 2021 The cophylab comet-simulation chamber *Rev. Sci. Instrum.* **92** 115102
Landau L D and Lifshitz E L 1987 *Fluid Mechanics* vol 6, 2nd edn (Amsterdam: Elsevier)
Larsson S, Prieto J M R, Gustafsson G, Häggblad H Å and Jonsén P 2020 The particle finite element method for transient granular material flow: modelling and validation *Comput. Part. Mech.* **8** 135–55
Lethuillier A, Le Gall A, Hamelin M, Schmidt W, Seidensticker K J, Grard R, Ciarletti V, Caujolle-Bert S, Fischer H-H and Trautner R 2016 Electrical properties and porosity of the first meter of the nucleus of 67P/Churyumov-Gerasimenko—as constrained by the permittivity probe SESAME-PP/Philae/Rosetta *Astron. Astrophys.* **591** A32
Miguel A F and Serrenho A 2007 On the experimental evaluation of permeability in porous media using a gas flow method *J. Phys. D: Appl. Phys.* **40** 6824–8
Pant L M, Mitra S K and Secanell M 2012 Absolute permeability and Knudsen diffusivity measurements in PEMFC gas diffusion layers and micro porous layers *J. Power Sources* **206** 153–60
Persad A H and Ward C A 2016 Expressions for the evaporation and condensation coefficients in the Hertz-Knudsen relation *Chem. Rev.* **116** 7727–67
Prialnik D 1991 A model of gas flow through comet nuclei *Theoretical Modelling of Comet Simulation Experiments* ed N Kömle, S Bauer and T Spohn (Vienna: Austrian Academy of Sciences Press)
Reshetnik V, Skorov Y, Bentley M, Rezac L, Hartogh P and Blum J 2022 Transport characteristics of a hierarchical near-surface layer of the nucleus of comet 67P/Churyumov–Gerasimenko *Sol. Syst. Res.* **56** 100–21
Reshetnyk V, Skorov Y, Vasyuta M, Bentley M, Rezac L, Agarwal J and Blum J 2021 Transport characteristics of the near-surface layer of the nucleus of comet 67P/Churyumov–Gerasimenko *Sol. Syst. Res.* **55** 106–23
Riffert 2022 Metallwaren Bienenzuchtgeräte Riffert (available at: www.metallwaren-riffert.at/siebgewebe.htm)
Sampson R A and Greenhill A G 1891 XII. On Stokes's current function *Phil. Trans. R. Soc.* A **182** 449–518
Satterfield C N 1970 *Mass Transfer in Heterogeneous Catalysis* (Cambridge, MA: MIT Press)
Schweighart M, Macher W, Kargl G, Gundlach B and Capelo H L 2021 Viscous and Knudsen gas flow through dry porous cometary analogue material *Mon. Not. R. Astron. Soc.* **504** 5513–27
Sharma S and Siginer D A 2010 Permeability measurement methods in porous media of fiber reinforced composites *Appl. Mech. Rev.* **63** 020802
Shen W, Song F, Hu X, Zhu G and Zhu W 2019 Experimental study on flow characteristics of gas transport in micro- and nanoscale pores *Sci. Rep.* **9** 10196
Skorov Y, Lieshout R V, Blum J and Keller H 2011 Activity of comets: gas transport in the near-surface porous layers of a cometary nucleus *Icarus* **212** 867–76
Skorov Y, Reshetnyk V, Bentley M, Rezac L, Agarwal J and Blum J 2020 The effect of varying porosity and inhomogeneities of the surface dust layer on the modelling of comet gas production *Mon. Not. R. Astron. Soc.* **501** 2635–46
Skorov Y, Reshetnyk V, Bentley M, Rezac L, Hartogh P and Blum J 2022 The effect of hierarchical structure of the surface dust layer on the modelling of comet gas production *Mon. Not. R. Astron. Soc.* **510** 5520–34
Spohn T *et al* 2015 Thermal and mechanical properties of the near-surface layers of comet 67P/Churyumov-Gerasimenko *Science* **349** aab0464
Steiner G, Kömle N and Kührt E 1991 Thermal modelling of comet simulation experiments *Theoretical Modelling of Comet Simulation Experiments* ed N Kömle, S Bauer and T Spohn (Vienna: Austrian Academy of Sciences Press)
Thomas N *et al* 2015 Redistribution of particles across the nucleus of comet 67P/Churyumov-Gerasimenko *Astron. Astrophys.* **583** A17
van Doormaal M A and Pharoah J G 2009 Determination of permeability in fibrous porous media using the lattice Boltzmann method with application to PEM fuel cells *Int. J. Numer. Methods Fluids* **59** 75–89
Weissberg H L 1962 End correction for slow viscous flow through long tubes *Phys. Fluids* **5** 1033–6
Wu Y-S, Pruess K and Persoff P 1998 Gas flow in porous media with Klinkenberg effects *Transp. Porous Media* **32** 117–37